

Automatic Optical Coherence Tomography Imaging of Stationary and Moving Eyes with a Robotically-Aligned Scanner

Mark Draelos, Pablo Ortiz, Ruobing Qian, Brenton Keller, PhD,
Kris Hauser, PhD, Anthony Kuo, MD, and Joseph Izatt, PhD

Abstract—Optical coherence tomography (OCT) has found great success in ophthalmology where it plays a key role in screening and diagnostics. Clinical ophthalmic OCT systems are typically deployed as tabletop instruments that require chinrest stabilization and trained ophthalmic photographers to operate. These requirements preclude OCT diagnostics in bedbound or unconscious patients who cannot use a chinrest, and restrict OCT screening to ophthalmology offices. We present a robotically-aligned OCT scanner capable of automatic eye imaging without chinrests. The scanner features eye tracking from fixed-base RGB-D cameras for coarse and stereo pupil cameras for fine alignment, as well as galvanometer aiming for fast lateral tracking, reference arm adjustment for fast axial tracking, and a commercial robot arm for slow lateral and axial tracking. We demonstrate the system’s performance autonomously aligning with stationary eyes, pursuing moving eyes, and tracking eyes undergoing physiologic motion. The system demonstrates sub-millimeter eye tracking accuracy, 12 μm lateral pupil tracking accuracy, 83.2 ms stabilization time following step disturbance, and 9.7 Hz tracking bandwidth.

Index Terms—Medical robotics, optical coherence tomography, image stabilization

I. INTRODUCTION

Optical coherence tomography (OCT) for structural eye imaging has revolutionized diagnostics in ophthalmology. In contrast to fundus photography for the retina or slit-lamp examination for the anterior eye, OCT captures quantitative cross-sections (or “B-scans”) of eye structures which enable geometric measurements (Fig. 1a) and volumetric reconstructions. Consequently, OCT is routinely employed for evaluation of diabetic retinopathy, age-related macular degeneration, and glaucoma in the posterior segment, and for corneal topography and biometry in the anterior segment. The American Academy of Ophthalmology lists OCT in its “Preferred Practice Patterns” when non-invasive, objective imaging is required [1], [2].

OCT is often found in ophthalmology clinics as a tabletop instrument in dedicated photography suites where it serves as a screening and diagnostic tool. Like a slit-lamp exam, patients undergoing OCT place their head on a chinrest and gaze into the OCT scanner (Fig. 1b) for several minutes while a trained ophthalmic photographer carefully aligns the eye

and captures images. The chinrest functions as a stabilizer to reduce motion artifacts and a guide to facilitate alignment. While suitable for ambulatory, cooperative patients, this setup precludes OCT diagnostics in bedbound or unconscious patients where chinrest imaging is infeasible and in urgent evaluations where a trained operator is unavailable. Both conditions exist in emergency rooms where OCT has an unrealized role in neurologic evaluation, such as detecting the ophthalmic signs of intracranial trauma [3].

Moreover, we envision a potential expanded role for OCT in routine screening for eye disease, rather than as a diagnostic tool for evaluating already symptomatic patients. Unfortunately, primary care clinics, where most health screening is performed, lack the equipment and/or expertise necessary to obtain OCT volumes of sufficient quality. Staffing ophthalmic photographers at such clinics is uneconomical without high volume, yet routing patients through ophthalmology clinics as part of their annual physical is not only inefficient but also costly. To succeed as a widespread screening tool, OCT must be fool-proofed and automated for widespread deployment.

We present a robotically-aligned swept-source OCT scanner capable of automatically imaging eyes without chinrests and characterize its performance. We combine fixed-base eye tracking and scanner movement for coarse alignment with scanner-integrated pupil tracking and scan beam aiming for fine alignment to capture stabilized OCT volumes within a $200 \times 300 \times 150$ mm workspace. Our system exhibits sub-millimeter eye tracking accuracy, 12 μm lateral pupil tracking accuracy, 83.2 ms stabilization time following step disturbance, and 9.7 Hz tracking bandwidth. Using a mannequin outfitted with model eyes, we demonstrate highly repeatable imaging of stationary eyes and pursuit of eyes moving at up to 30 mm s^{-1} or undergoing simulated physiologic motion.

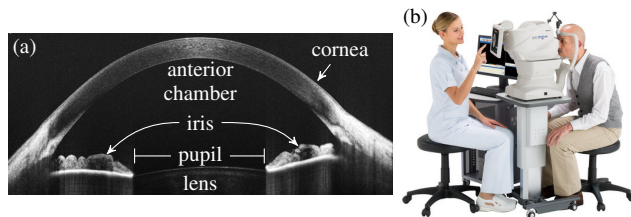


Fig. 1. (a) OCT B-scan of the anterior eye revealing the cornea, iris, and crystalline lens by Wasatch Photonics. (b) Commercial ophthalmic OCT system with patient chinrest and operator console by Topcon Medical Systems.

*This research is partially supported by NIH F30-EY027280, NIH R01-EY029302, and the Coulter Translational Partnership.

M. Draelos, P. Ortiz, R. Qian, B. Keller, and J. Izatt are with the Department of Biomedical Engineering, Duke University, Durham, NC, USA. K. Hauser is with the Department of Electrical and Computer Engineering, Duke University, Durham, NC, USA. A. Kuo is with the Department of Ophthalmology, Duke University Medical Center, Durham, NC, USA. mark.draelos@duke.edu

II. RELATED WORK

The benefits of self-aligning OCT systems have not escaped the notice of commercial OCT vendors. In efforts to increase image quality while reducing imaging time, major developers Zeiss, Topcon, and Canon offer ophthalmic OCT systems with integrated eye alignment and tracking that achieve lateral resolutions of 10–20 μm . Although such features lower the necessary operator skill level, these systems still rely on a chinrest for initial alignment and stabilization. Furthermore, they remain bulky tabletop instruments. Modern commercial OCT systems continue to lack the flexibility needed to image non-ambulatory patients without a trained operator.

Handheld OCT offers an attractive solution by compactly packaging the scan head and moving all other components into a tethered cart. Many research scanners [4]–[8] with vanishingly small form factors [9], and even a commercial offering by Leica Microsystems, make non-ambulatory imaging possible. Without a chinrest, however, a highly skilled operator is needed to manually align the scanner and maintain that alignment until acquisition completes, yielding very operator-dependent image quality. The chinrest’s mechanical limitation is merely replaced by an operator skill barrier.

Image registration in post-processing is perhaps the easiest way to compensate for varying alignment, especially that seen with handheld OCT [10], [11]. Frequently this is facilitated by additional imaging that measures the motion for later correction, such as with a scanning laser ophthalmoscope [12]. These approaches are fundamentally constrained by the original image quality and suffer from a small correction range. Moreover, the imaging depth of most OCT systems is less than 10 mm, outside which range correction is not possible because the image is entirely absent.

There is presently a large gap between the ease of commercial self-aligning OCT and the flexibility of handheld OCT. Our robot-mounted scanner bridges that gap by offering flexible and automatic alignment.

III. SYSTEM

Our robotically-aligned OCT scanner performs eye and pupil tracking and implements a controller to choose the best tracking source for alignment. Three distinct tracking modes are possible: the “eye” mode using the eye tracker exclusively, the “pupil” mode using the pupil tracker once the scanner is roughly aligned, and the “pupil+aiming” mode using the pupil tracker with error feedforward for scan aiming. In this initial development, we assumed forward-facing eyes moving no faster than those of a freestanding person attempting to hold still (e.g., about 20 mm s^{-1}). Section III-A introduces the scanner’s hardware, Section III-B describes the eye and pupil tracking algorithms, and Section III-C explains the system’s control strategies.

A. Hardware

Our scanner is composed of three subsystems: fixed-base eye tracking cameras, an OCT scanner with integrated pupil tracking cameras mounted on a robot arm, and an OCT

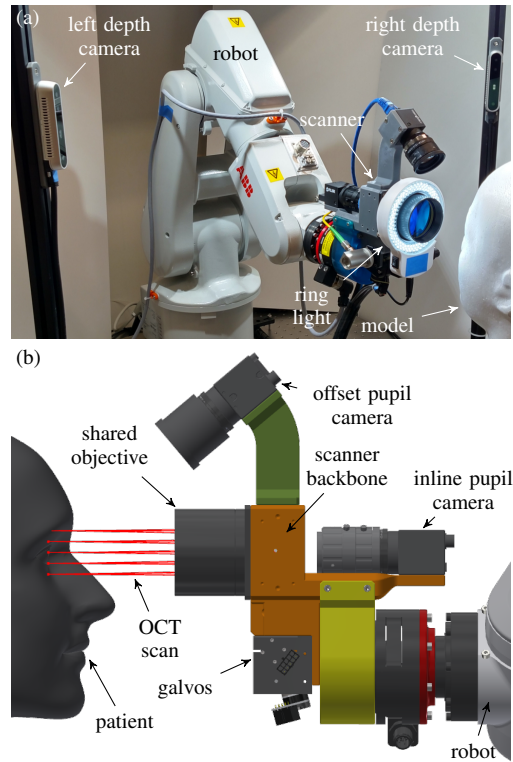


Fig. 2. Robotically-aligned scanner system (a) and scanner design (b). The lights mounted above each depth camera are not pictured.

engine with a motorized reference arm (Fig. 2). For eye tracking, we used two RealSense D415 RGB-D cameras (Intel; Santa Clara, CA), one for each eye, positioned symmetrically about the robot arm and aimed at the tracking workspace. These vantage points were chosen to obtain clear views of the designated eye (left eye for left camera and right eye for right camera), even with the scanner partially occluding the face during alignment. We calibrated each camera’s position in the robot’s coordinate system by imaging an ArUco [13] target mounted on the robot end-effector. An LED light above each camera was used for uniform, flicker-free illumination.

For OCT imaging, we designed a custom anterior eye OCT scanner with integrated pupil tracking cameras (Fig. 2b). The scanner and inline pupil camera shared a 2 in. objective lens with a 93 mm working distance to provide a comfortable separation for patients during automatic alignment. We used Saturn 1B galvanometers (Pangolin Laser Systems; Orlando, FL) with a 3.8 mm beam launched from a reflective collimator. A dichroic with a 700 nm cutoff folded the scanner into the inline pupil camera’s optical path. We optimized the optical design with OpticStudio (Zemax; Kirkland, WA) to achieve diffraction-limited OCT performance at 1060 nm over a $\pm 15\text{mm}$ field of view and 3D printed the scanner’s backbone to position all components in accordance with the optimization results. This yielded a theoretical lateral OCT resolution of 43 μm due to the scanner’s exaggerated working distance. The OCT field of view was co-registered to the

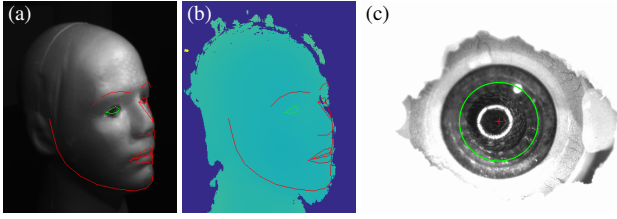


Fig. 3. Views from the right eye tracking camera in infrared (a) and colorized depth (b) with detected face outline (red/green), and inline pupil camera view (c) with detected pupil overlay (red/green).

inline pupil camera using galvanometer voltage offsets. A second offset pupil camera was included to create a stereo pair for pupil depth estimation. We used a Blackfly S 04S2M camera and a Blackfly 13E4C camera (FLIR; Richmond, BC, Canada) for the inline and offset pupil cameras, respectively. A ring light was mounted on the objective lens housing to provide uniform illumination and eliminate shadows under the eyebrow for pupil tracking. The whole scanner weighed approximately 1.1 kg. We used an IRB 120 robot arm (ABB Robotics; Zürich, Switzerland) controlled at 250 Hz through its Externally Guided Motion interface for scanner positioning with $10\mu\text{m}$ repeatability to demonstrate the robotic alignment concept.

We operated the scanner with a custom-built swept-source OCT engine. The OCT engine used a 1060 nm swept frequency source (Axsun Technologies; Billerica, MA) with 100 nm bandwidth at a 100 kHz A-scan rate and an A-LSQ150D-E01 linear stage (Zaber Technologies; Vancouver, BC, Canada) to adjust the reference arm length. The optical signal detection chain used a 800MS^{-1} digitizer (AlazarTech; Quebec, Canada) to measure the output of a balanced photoreceiver (Thorlabs; Newton, NJ). The engine provided an imaging depth of up to 7.4 mm, suitable for imaging the complete anterior chamber. We acquired OCT volumes at 0.3 Hz using a $512 \times 1376 \times 512$ voxel raster scan pattern which had physical dimensions of $12 \times 7.4 \times 12$ mm. Galvanometer aiming offsets were generated using a NI-9263 analog output module (National Instruments; Austin, TX) and added to the engine’s scan waveforms by a custom summing circuit. The adjustable reference arm and galvanometer offsets enabled the aiming portion of the pupil+aiming mode. We performed real-time OCT processing and rendering on the graphics processing unit with custom software.

B. Tracking

1) *Eye*: We tracked the eye’s 3D position in the robot’s coordinate system by identifying faces in the RealSense D415s’ left stereo image using OpenFace 2.0 [14] in video tracking mode (Fig. 3a-b). We chose OpenFace because it handled partial face occlusions robustly. By manually tuning the exposure and illumination, we obtained left stereo images suitable for face tracking, despite the presence of the D415s’ active stereo texture, without compromising depth imaging. Because the D415s generate depth images from the left stereo viewpoint, detected facial landmarks were thus also valid in

the depth image without the need for reprojection. We estimated the eye’s 3D position by computing the mean position of all depth pixels bounded by the facial landmarks for the eye of interest. Eye tracking operated at approximately 38 fps for the right and left eye tracking cameras together for input images sized 848×480 pixels.

2) *Pupil*: We tracked the pupil’s 3D position in the inline pupil camera’s coordinate system by triangulating the pupil seen in both the inline and offset pupil cameras. Using the methods from [15], we identified the pupil in the inline pupil camera’s view by adaptively thresholding the image and finding the largest connected component (CC) with a roughly square aspect ratio. We estimated the pupil’s pixel position as that CC’s bounding box center because the CC frequently did not include the entire pupil interior and thus biased the CC’s centroid away from the true center. We then projected the ray from the inline pupil camera through the pupil center onto the offset pupil camera’s image and performed a line search for the pupil. This yielded the pupil position in 3D space relative to the scanner. Inline pupil camera processing operated at 230 fps whereas offset pupil camera processing operated at 140 fps due to a hardware framerate limitation. We matched the two cameras’ framerates using a zero-order hold.

C. Controller

The controller performed alignment in a two-stage, high-level strategy. First, it positioned the scanner to bring the desired eye into the inline pupil camera’s field of view using the coarse eye position from the fixed-base eye tracking cameras. Second, once the inline pupil camera reported pupil detection, the controller positioned the scanner exclusively using the fine eye position from pupil tracking. This strategy enabled a large workspace without compromising fine alignment.

We implemented this strategy in a state machine that selectively engaged eye and pupil tracking as well as tolerated tracking failures for both (Fig. 4). If eye tracking failed, either because no patient was present or because the scanner occluded the patient’s face, the robot moved the scanner to a “recovery” position (Fig. 4a) to prevent occlusions. If

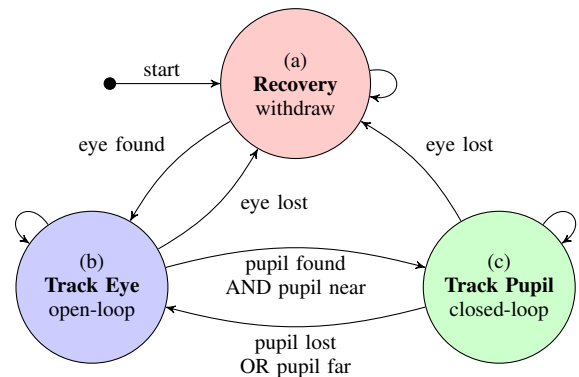


Fig. 4. Controller state transition diagram for autonomous, fault-tolerant eye alignment.

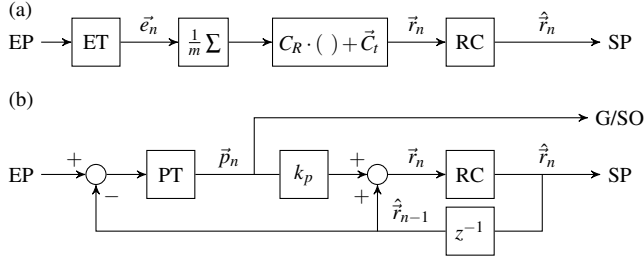


Fig. 5. Control diagram for open-loop eye tracking (a) and for closed-loop pupil tracking (b) with galvanometer/reference arm feedforward. EP = eye position, ET = eye tracker, PT = pupil tracker, RC = robot controller, SP = scanner position, and G/SO = galvanometer/stage offset.

pupil tracking failed or the estimated pupil position deviated significantly from the scanner’s current position, the robot tracked only the coarse eye position (Fig. 4b). The deviation check prevented incorrectly tracking the wrong eye, for instance, if the pupil camera passed over the left eye while the robot moved to position the scanner to view the right eye. Otherwise, the scanner relied on pupil tracking (Fig. 4c) for fine alignment.

The controller applied distinct control methods for the eye and pupil tracking states. During eye tracking, the controller issued open-loop position setpoints \vec{r}_n to the robot arm (Fig. 5a) after smoothing the eye position \vec{e}_n with an m -sample moving average filter,

$$\vec{r}_n = C_R \cdot \left(\frac{1}{m} \sum_{i=0}^{m-1} \vec{e}_{n-i} \right) + \vec{C}_t, \quad (1)$$

where C is the camera pose and $m = 15$. No feedback was possible because the scanner position did not affect the estimated eye position except in the undesired case of face occlusion. During pupil tracking, the controller implemented a feedback loop to eliminate the tracking error \vec{p} because the pupil cameras were referenced to the robot arm (Fig. 5b). The controller applied proportional gain k_p to drive the robot arm’s position setpoints,

$$\vec{r}_n = \hat{r}_{n-1} + k_p \vec{p}_n \quad (2)$$

where \hat{r} is the robot arm’s actual position and $k_p = 0.4$, and fed the error signal forward as a galvanometer scan offset and motorized reference arm setpoint (i.e., “aiming” in the pupil+aiming mode). While the robot tracked the eye with “low” bandwidth, the galvanometers and reference arm stage rapidly corrected the residual error with “high” bandwidth. This low bandwidth tracking centered the galvanometers and reference arm within their operating range to ensure the availability of high bandwidth tracking except for large eye motion.

For all robot motions, the controller generated time optimal trajectories in Cartesian space each control cycle (4 ms) to bring the scanner to its desired position. We enforced a maximum velocity of 100 mm s^{-1} in each dimension to avoid startling patients.

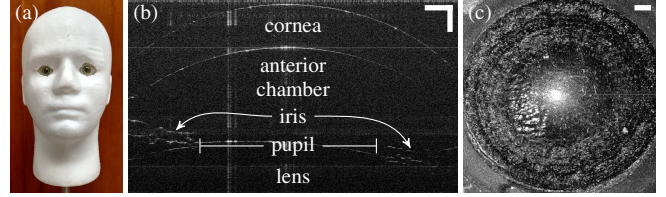


Fig. 6. (a) Styrofoam mannequin head fitted with model eyes. (b) OCT B-scan through the model eye’s center showing its anatomically realistic structures. (c) OCT *en face* maximum intensity projection constructed from successive adjacent B-scans. Scale bars are 1 mm.

IV. METHODS

We performed an evaluation of our automatic alignment system using a Styrofoam mannequin head fitted with Okulo GR-6 model eyes (BIONIKO; Miami, FL) that included an anatomically realistic cornea, iris, and anterior chamber (Fig. 6). We chose mannequins over human subjects for testing because doing so provided the necessary standardization and precision. We defined successful alignment according to clinical OCT imaging practice: laterally center the pupil and axially position the corneal apex near zero OCT depth. These tests evaluated performance aligning stationary eyes, pursuing moving eyes, and tracking eyes exhibiting common physiologic motions. Except for tracking accuracy and precision assessments, we performed all tests in the three possible tracking modes: eye, pupil, and pupil+aiming. Testing in this way elicited the effect of each successive technique.

A. Tracking Performance

We examined both eye and pupil tracking to determine their accuracy and precision. For eye tracking, we positioned the mannequin near the tracking workspace center facing the robot arm without the scanner. We then moved the head laterally and axially in steps of 25 mm using a linear stage. Tracking precision was calculated using the standard deviation of the estimated eye position at each step. Tracking accuracy was calculated using the standard deviation of the error in estimated position displacement. For pupil tracking, we manually aligned the mannequin’s left eye with the scanner. We then performed the same measurements as with eye tracking above but using 1 mm steps.

B. Alignment Performance

To assess the controller’s ability to obtain consistent OCT volumes of stationary eyes, we performed alignment with the mannequin’s left eye at three different positions spaced 50 mm apart. Each attempt started from the recovery position. We recorded the time to alignment and acquired an OCT volume at $512 \times 1376 \times 512$ voxels once alignment had stabilized. Additionally, we elicited the system’s tracking step response by rapidly shifting the eye laterally by approximately 5 mm using a linear stage midway through an OCT volume acquisition. We recorded the scanner position and pupil tracking error during the response, as well as the interrupted OCT volume.

TABLE I
TRACKING PRECISION AND ACCURACY

Metric	Right Eye Tracking (μm)		Left Eye Tracking (μm)		Pupil Tracking (μm)	
	Lateral	Axial	Lateral	Axial	Lateral	Axial
Precision	130	82	130	100	6.3	64
Accuracy	280	580	310	840	12	170

C. Standardized Motion

To assess the controller’s ability to obtain OCT volumes of moving eyes, we performed automatic alignment while the mannequin’s left eye was moved at 10 mm s^{-1} , 20 mm s^{-1} , and 30 mm s^{-1} on a linear stage for 150 mm. While the system’s intended use case does not include pursuit of eyes moving so rapidly for such a distance, this test served to demonstrate performance for extreme patient motion. We recorded the scanner position, pupil tracking error, and continuous OCT volumes at $512 \times 1376 \times 512$ voxels (0.3 Hz) during the pursuit. All tests started with the system initially aligned to the eye.

D. Physiologic Motion

To assess the controller’s ability to obtain OCT images of eyes undergoing physiologic movement, the mannequin head was held with an outstretched arm within the tracking workspace. This allowed physiologic motions such as tremor, pulse, and respiration to propagate to the mannequin. We recorded a set of OCT volumes at $512 \times 1376 \times 512$ voxels (0.3 Hz) once alignment had initially stabilized.

V. RESULTS

Table I and Fig. 7 show the results of the tracking precision and accuracy evaluation. The eye trackers demonstrated sub-millimeter accuracy whereas the pupil tracker demonstrated $12\text{ }\mu\text{m}$ lateral and $170\text{ }\mu\text{m}$ axial accuracy. Figure 8 shows the step response of the system using each tracking mode. The robot exhibited a control lag of approximately 50 ms. Using rise times (10% \rightarrow 90%) to estimate bandwidth, the tracking modes exhibited 1.1 Hz and 9.7 Hz lateral response bandwidth with and without aiming, respectively. The numbers of B-scans before alignment reestablished were 90, 60, and 13 for the eye, pupil, and pupil+aiming modes, respectively. At 6.4 ms per B-scan, this corresponded to 576 ms, 384 ms, and 83.2 ms settling times, respectively.

Figure 9 shows repeated OCT B-scans and *en face* maximum intensity projections (MIPs) of the same eye for different model positions using each tracking mode. Each alignment completed in under 15 s which included scanner advancement, volume acquisition time of approximately 3 s, and scanner retraction. Eye tracking alone failed to stably center on the pupil whereas pupil tracking without aiming was sufficient to do so.

Figure 10 shows the best (i.e., brightest with least motion artifact) OCT B-scans and MIPs obtained during the linear pursuit tests. Eye tracking only did not yield usable results.

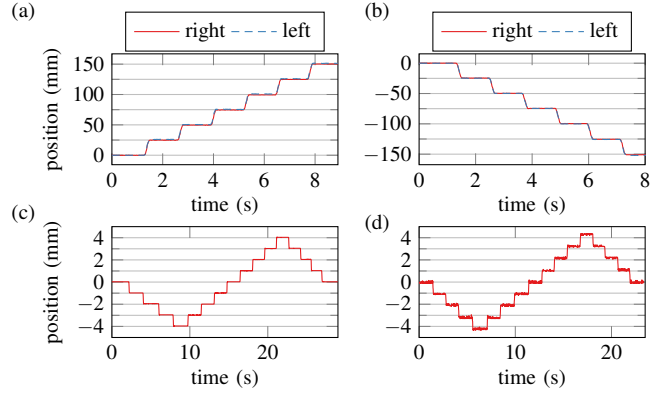


Fig. 7. Accuracy test results for lateral (a) and axial (b) eye tracking with 25 mm steps and lateral (c) and axial (d) pupil tracking with 1 mm steps.

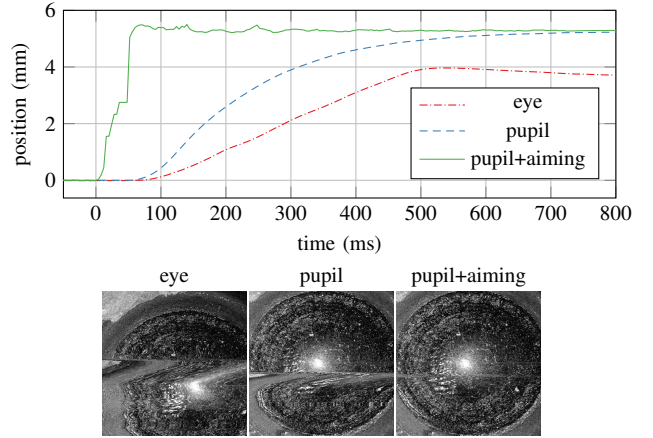


Fig. 8. Step response for lateral displacement in OCT scan center position (i.e., robot position + galvanometer offset) with corresponding interrupted OCT scans for each tracking mode.

Pupil tracking yielded usable scans at 10 mm s^{-1} , despite sub-optimal axial alignment. Pupil tracking with aiming yielded usable scans at all three velocities. Figure 11 shows the best of four successive OCT scans obtained during the physiologic motion test using each tracking mode. Only pupil tracking with aiming obtained a reasonable OCT scan, despite the presence of high frequency lateral noise.

VI. DISCUSSION

Our robotically-aligned OCT scanner produced encouraging results in all tests. Both the eye and pupil trackers exhibited appropriate baseline accuracy and precision for maintaining alignment. Although not suitable for fine alignment, the eye tracker accuracy was sufficient to bring the eye into the pupil tracker’s field of view. In contrast, the lateral pupil tracking accuracy of $12\text{ }\mu\text{m}$ is below the OCT scanner’s lateral resolution; the repeated scans in Fig. 9’s bottom two rows would be indistinguishable except for small changes in reflection and scan artifacts. The axial pupil tracking accuracy and precision would benefit from an order of magnitude improvement, however, as that would reduce reference arm adjustment chatter and move the alignment

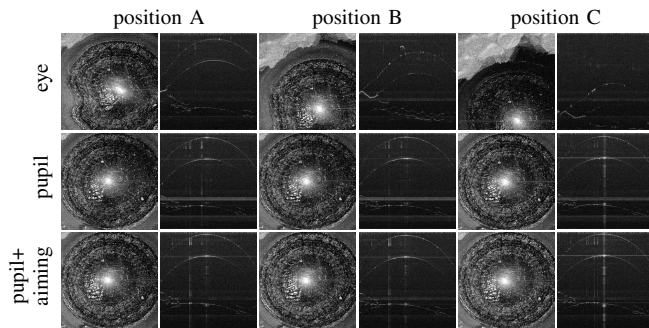


Fig. 9. OCT MIPs and middle B-scans at three different model positions (columns) spaced 50 mm apart for each tracking mode (rows).

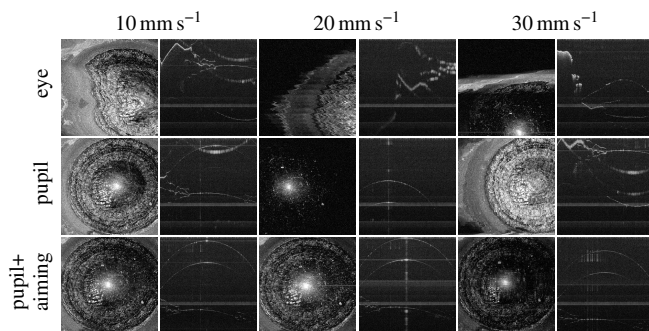


Fig. 10. Best OCT MIPs and middle B-scans during linear pursuit for each tracking mode (rows) at different velocities (columns).

accuracy closer to the OCT engine’s axial resolution of roughly $10\mu\text{m}$. This can likely be achieved by optimizing the offset pupil camera lens and resolution.

Supplementing pupil tracking with galvanometer aiming achieved a significant improvement in the scanner’s step response in Fig. 8, nearly a factor of nine as measured by tracking bandwidth. The identical bandwidth for the eye and pupil modes suggests that the robot is a common limiting factor. Whereas both the eye and pupil modes require the robot to physically move the scanner, the pupil+aiming mode needs only to tweak the galvanometers which are already sweeping across the eye at 150Hz for these OCT scans. In addition to a slower step response, the robot controller also introduces latency which is overcome by the high-speed galvanometer drivers, so much so that the galvanometers have nearly settled before the robot begins moving.

Based on tracking performance tests, the linear pursuit results are unsurprising. Eye tracking alone fails to center the pupil and lags significantly, giving largely useless OCT scans. Adding pupil tracking yields stabilized OCT scans, but the low response bandwidth manifests as an off-center scan with poor axial alignment. The full tracking package with galvanometer aiming and reference arm adjustment eliminates any suggestion of motion (comparing Fig. 9 and Fig. 10 bottom rows) for the 10mm s^{-1} and 20mm s^{-1} cases. At 30mm s^{-1} , the reference arm adjustment becomes limiting, as evidenced by the darkened MIP and shifted B-scan, although the MIP shows high frequency lateral noise

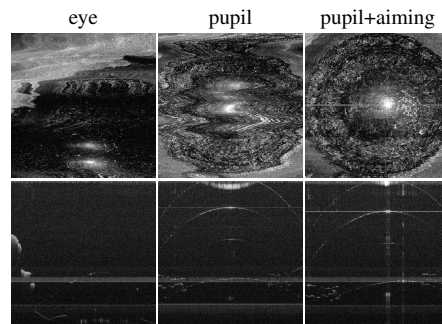


Fig. 11. Best OCT MIPs and middle B-scans for each tracking mode (columns) when holding the mannequin with an outstretched arm to simulate physiologic motion.

too. Unfortunately, a motorized reference arm stage will inherently perform less well than galvanometers due to its higher inertia.

The handheld mannequin test in Fig. 11 is closest to our intended application of aligning with unstabilized eyes. Eye tracking only effectively models an operator trying to align a handheld OCT scanner without seeing the acquired scan. The resulting OCT volume is off-center and useless when captured by human or robot. Pupil tracking alone models the same scenario but with alignment feedback, which proves to be insufficient for following the moving eye. Pupil tracking with galvanometer aiming allows the scanner to automatically target the pupil in the presence of small misalignments. The obtained scans are usable; however, lateral high frequency noise is visible in the MIP as it was for 30mm s^{-1} pursuit. Nevertheless, this result indicates that our system has potential for imaging *in vivo* eyes without chinrests.

Several obstacles remain for deploying a system such as this to a clinic. First, the IRB 120 robot arm used here for demonstration is suboptimal from a weight and safety standpoint. Using lighter, collaborative robot arms is preferable and will increase the viability of this approach. Moreover, galvanometer aiming reduces the need for high-performance robot motion. Second, imaging actual patients is significantly more complicated than imaging mannequins. Real patients exhibit a number of behaviors that interfere with tracking, such as turning their heads and blinking. More robust face tracking to detect such conditions and reliably withdraw the scanner is needed to make a robotically positioned scanner practical. Third, fixed-base eye tracking like that used here will likely fail for bedbound patients due to field of view challenges. Movable eye tracking cameras that automatically calibrate their position can address this.

VII. CONCLUSION

We have demonstrated a proof-of-concept robotically-aligned OCT scanner that can image both stationary and moving eyes without operator intervention. The combination of eye tracking, pupil tracking, galvanometer aiming, and reference arm adjustment enables a large functional workspace without compromising fine alignment.

REFERENCES

- [1] AAO PPP Retina/Vitreous Panel, Hoskins Center for Quality Eye Care, "Diabetic Retinopathy PPP," American Academy of Ophthalmology, 2017.
- [2] AAO Cornea/External Disease PPP Panel, Hoskins Center for Quality Eye Care, "Corneal Edema and Opacification PPP," American Academy of Ophthalmology, 2013.
- [3] M. C. Walker and M. D. O'Brien, "Neurological examination of the unconscious patient," *J R Soc Med*, vol. 92, no. 7, pp. 353–355, Jul 1999.
- [4] S. Radhakrishnan, A. M. Rollins, J. E. Roth, S. Yazdanfar, V. Westphal, D. S. Bardenstein, and J. A. Izatt, "Real-time optical coherence tomography of the anterior segment at 1310 nm," *Arch. Ophthalmol.*, vol. 119, no. 8, pp. 1179–1185, Aug 2001.
- [5] W. Jung, J. Kim, M. Jeon, E. J. Chaney, C. N. Stewart, and S. A. Boppart, "Handheld optical coherence tomography scanner for primary care diagnostics," *IEEE Trans Biomed Eng*, vol. 58, no. 3, pp. 741–744, Mar 2011.
- [6] C. D. Lu, M. F. Kraus, B. Potsaid, J. J. Liu, W. Choi, V. Jayaraman, A. E. Cable, J. Hornegger, J. S. Duker, and J. G. Fujimoto, "Handheld ultrahigh speed swept source optical coherence tomography instrument using a MEMS scanning mirror," *Biomed Opt Express*, vol. 5, no. 1, pp. 293–311, Dec 2013.
- [7] D. Nankivil, G. Waterman, F. LaRocca, B. Keller, A. N. Kuo, and J. A. Izatt, "Handheld, rapidly switchable, anterior/posterior segment swept source optical coherence tomography probe," *Biomed Opt Express*, vol. 6, no. 11, pp. 4516–4528, Nov 2015.
- [8] J. Yang, L. Liu, J. P. Campbell, D. Huang, and G. Liu, "Handheld optical coherence tomography angiography," *Biomed Opt Express*, vol. 8, no. 4, pp. 2287–2300, Apr 2017.
- [9] F. LaRocca, D. Nankivil, T. DuBose, C. A. Toth, S. Farsiu, and J. A. Izatt, "In vivo cellular-resolution retinal imaging in infants and children using an ultracompact handheld probe," *Nat Photonics*, vol. 10, pp. 580–584, 2016.
- [10] S. Ricco, M. Chen, H. Ishikawa, G. Wollstein, and J. Schuman, "Correcting motion artifacts in retinal spectral domain optical coherence tomography via image registration," in *International Conference on Medical Image Computing and Computer-Assisted Intervention (MICCAI)*. Springer, 2009, pp. 100–107.
- [11] M. F. Kraus, B. Potsaid, M. A. Mayer, R. Bock, B. Baumann, J. J. Liu, J. Hornegger, and J. G. Fujimoto, "Motion correction in optical coherence tomography volumes on a per A-scan basis using orthogonal scan patterns," *Biomed Opt Express*, vol. 3, no. 6, pp. 1182–1199, 2012.
- [12] A. G. Capps, R. J. Zawadzki, Q. Yang, D. W. Arathorn, C. R. Vogel, B. Hamann, and J. S. Werner, "Correction of eye-motion artifacts in AO-OCT data sets," in *Ophthalmic Technologies XXI*, vol. 7885. International Society for Optics and Photonics, 2011, p. 78850D.
- [13] S. Garrido-Jurado, R. M. noz Salinas, F. Madrid-Cuevas, and M. Marín-Jiménez, "Automatic generation and detection of highly reliable fiducial markers under occlusion," *Pattern Recognition*, vol. 47, no. 6, pp. 2280–2292, 2014.
- [14] A. Zadeh, Y. C. Lim, T. Baltrušaitis, and L. Morency, "Convolutional experts constrained local model for 3D facial landmark detection," in *2017 IEEE International Conference on Computer Vision Workshops (ICCVW)*, Oct 2017, pp. 2519–2528.
- [15] O. Carrasco-Zevallos, D. Nankivil, B. Keller, C. Viehland, B. J. Lujan, and J. A. Izatt, "Pupil tracking optical coherence tomography for precise control of pupil entry position," *Biomed Opt Express*, vol. 6, no. 9, pp. 3405–3419, Sep 2015.